

Advanced Physics Laboratory

Lattice Vibrations and Effects of Free Charge Carriers in
Solids

Name: Nicolò De Masi, Manthan Chattopadhyay

Experiment Date: 14.05.2024



Abstract

This report investigates the spectral dependence of optical parameters in solids, focusing on lattice vibrations and the effects of free charge carriers using infrared (IR) spectroscopy. Upon proper calibration of the spectrometer's wavenumber scale, transmission and reflectivity spectrum of Al_2O_3 is examined to determine characteristic quantities such as dielectric function, energy of phonon modes, background dielectric constant (ϵ_∞), damping constant, as well as substrate thickness. A similar treatment is done for Si, while ZnO thin film's phonon properties are characterized, assuming transparency and negligible backside reflection. Lastly, the reflectivity spectrum of n-doped GaAs is measured to estimate the concentration of free charge carriers and plasmon frequency (ω_p).

Contents

1 Theoretical Background	4
1.1 The Dielectric Function	4
1.2 Lattice Vibrations & Phonon Dispersion	6
1.3 Optical Response of Bound Charges: Lorentz Oscillator	8
1.4 Effects of Free Charge Carriers	10
1.5 Complex Refractive Index & Absorption	11
1.6 Reflectance and Transmittance	11
1.7 Fourier Transform Infrared Spectroscopy (FTIR)	14
1.8 Spectral Analysis	16
2 Experimental Setup	18
3 Results & Discussion	20
3.1 Task 1: Calibration of the wave-number scale	20
3.1.1 Water vapor	20
3.1.2 Polystyrene foil	21
3.2 Task 2: Glass and NaCl blocking filters	23
3.2.1 Glass	23
3.2.2 NaCl	25
3.3 Task 3: Reflectivity and Transmission spectrum of Sapphire	26
3.3.1 Reflectivity Spectrum and Dielectric Function	26
3.3.2 Transmission Spectrum and sample thickness	31
3.4 Task 4: Optical properties of Silicon	32
3.4.1 Absorbance	33
3.4.2 Absorption (α) and Extinction (κ) coefficients	34
3.5 Task 5: Phonon properties of ZnO Thin Film	35
3.6 Task 6: Free Charge Carriers Asborption in GaAs	39
4 Conclusion & Outlook	41

1 Theoretical Background

IR spectroscopy was pioneered by William Weber Coblenz in the early 1900s. He demonstrated that chemical functional groups exhibit specific and characteristic IR absorption [1]. The infrared portion of the electromagnetic spectrum is divided into three regions - the near-, mid- and far-infrared. The higher-energy near-IR, with wavenumber approximately 14,000-4,000 cm⁻¹ can excite combination modes of molecular vibrations, while the mid-IR, approximately 4,000-400 cm⁻¹ is used to study fundamental vibrations and associated rotational-vibrational structure. Far-IR with wavenumber 400-10 cm⁻¹ has the lowest energy with applications in studying low frequency vibrations [2]. Here we study nearly isotropic materials in the range 4000-200 cm⁻¹.

Upon measurement of the transmission and reflectivity spectrum, we determine the frequency dependence of optical parameters. The subsequent sections provide the necessary literature to understand the frequency dependence of these parameters.

1.1 The Dielectric Function

The dielectric permittivity (ε) of a crystal describes its response to an external electric field \mathbf{E} . The onset of an electric polarisation \mathbf{P} and corresponding displacement field \mathbf{D} in the material can be characterised by

$$\mathbf{D} = \varepsilon \varepsilon_0 \mathbf{E} = \varepsilon_0 \mathbf{E} + \mathbf{P} \quad (1)$$

due to subsequent creation of local dipoles and their alignment within the crystal; ε_0 is the vacuum permittivity. In general ε is a rank two tensor described by a 3×3 matrix, but can be thought of as a scalar for isotropic cubic materials. Polarisation with units C/m^2 is defined as the dipole moment per unit volume, $P = n_d \mu_d$ where n_d is the dipole concentration and μ_d the moment of a single dipole. One also defines a dielectric susceptibility that quantifies the strength of induced \mathbf{P} ,

$$\chi_e = \frac{P}{\varepsilon_0 E} \implies \varepsilon = 1 + \chi_e \quad (2)$$

Upon exposure to an oscillating field $E = E_0 e^{-i\omega t}$, the in-phase and out-of-phase polarisation is depicted by frequency-dependent complex permittivity and susceptibility.

$$\varepsilon(\omega) = \varepsilon' + i\varepsilon'' \quad (3)$$

Considering Maxwell's equation in the absence of a magnetic field,

$$\mathbf{j} = -\frac{\partial \mathbf{D}}{\partial t} = -\varepsilon_0 \omega (i\varepsilon' - \varepsilon'') \mathbf{E} = \mathbf{j}_\perp + \mathbf{j}_\parallel \quad (4)$$

Thus ε' describes displacement of material polarisation, while ε'' is a measure of joule heating given by $\mathbf{E} \cdot \mathbf{j}$. From equation (1) it follows that

$$P = (\varepsilon' - 1) E_0 e^{-i\omega t} + \varepsilon'' E_0 e^{-i\omega t} \quad (5)$$

The effect of a sudden change in applied electric field on polarisation compromises of a delay due to the rotation of atoms and molecules taking a finite time before alignment with the field. Assuming exponential nature of relaxation, with

characteristic relaxation time τ , ε'' shows a peak-like structure with maximum at $\omega = 1/\tau$.

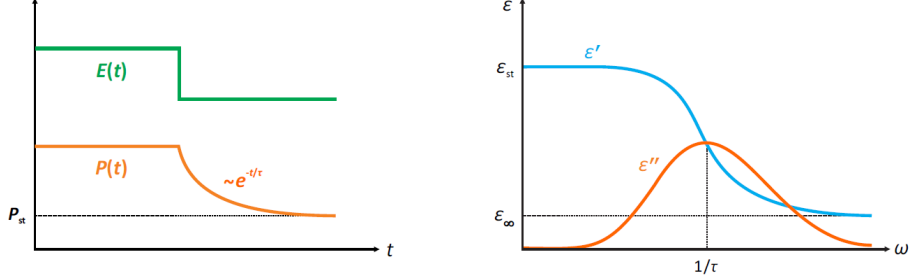


Figure 1: Debye model of relaxation. Left: abrupt change in E induces an exponential change in polarisation. Right: real and imaginary parts of ε as a function of frequency [3]

ε' approaches static permittivity ε_{st} at low frequencies, whereas $\varepsilon'' \rightarrow 0$. In the high frequency regime, ε' approaches the background dielectric noise ε_∞ , while ε'' again vanishes.

As can be inferred from shown relations, the real and complex part of the dielectric function $\varepsilon(\omega)$ are not independent of each other due to fundamental principle of causality. This implies that response of a system (eg. polarisation) can not precede the external perturbation (eg. applied electric field), thereby imposing a constraint on $\varepsilon(\omega)$, leading to the Kramers-Kronig relations given by:

$$\begin{aligned}\varepsilon'(\omega) &= 1 + \frac{2}{\pi} \mathcal{P} \int_0^\infty \frac{\omega' \varepsilon''(\omega')}{\omega'^2 - \omega^2} d\omega' \\ \varepsilon''(\omega) &= -\frac{2\omega}{\pi} \mathcal{P} \int_0^\infty \frac{\varepsilon'(\omega')}{\omega'^2 - \omega^2} d\omega'\end{aligned}\quad (6)$$

where \mathcal{P} is the principal value of the integral [5].

In the far and mid-IR range investigated in this report, the dielectric function experiences contribution from both free charge carriers (χ^P), and lattice vibrations (χ^L) such that,

$$\varepsilon = \varepsilon_\infty + \chi^P + \chi^L \quad (7)$$

1.2 Lattice Vibrations & Phonon Dispersion

A typical interatomic potential is depicted below:

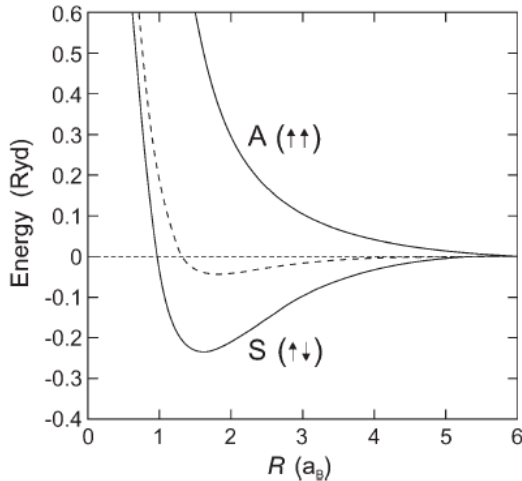


Figure 2: Binding of the hydrogen molecule. *Dashed Line*: classical electrostatic calculation, 'S', 'A': quantum-mechanical calculation taking into account Pauli's principle (S: symmetric orbital, anti-parallel spins, A: anti-symmetric orbitals, parallel spins) [4]

The atoms in a solid are elastically bonded and have an average position from which they deviate. From Figure 2, we note that the atom performs vibrational motion and the solid is elastic. This enables us to perform a harmonic approximation around the minimum. Note that beyond the elastic regime, plastic deformations (irreversible) such as dislocations also occur [4].

In this section we will discuss the dispersion relation for lattice vibration of a linear (1D) diatomic chain.

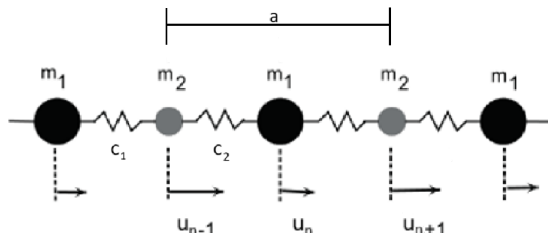


Figure 3: Schematic of diatomic linear chain [6]

Alternating atoms of species 1 and 2 are placed on the chain with C_1 being the spring constant for the 1-2 bond within the base, and C_2 the spring constant for 2-1 bond between different bases. The displacements of the atoms are labeled u_n^1 and u_n^2 with both belonging to lattice point n .

The total energy of the system is given as

$$U = \frac{1}{2}C_1 \sum_n (u_n^1 - u_n^2)^2 + \frac{1}{2}C_2 \sum_n (u_n^2 - u_{n+1}^1)^2 \quad (8)$$

resulting in equations of motion

$$\begin{aligned} M_1 \ddot{u}_n^1 &= -C_1(u_n^1 - u_n^2) - C_2(u_n^1 - u_{n-1}^2) \\ M_2 \ddot{u}_n^2 &= -C_1(u_n^2 - u_n^1) - C_2(u_n^2 - u_{n+1}^1) \end{aligned} \quad (9)$$

By applying the plane wave ansatz $u_n^{1,2}(x, t) = v_{1,2} \exp\{i(kna - \omega t)\}$ and periodic boundary condition

$$\begin{aligned} 0 &= -M_1 \omega^2 v_1 + C_1(v_1 - v_2) + C_2[v_1 - v_2 \exp\{-ika\}] \\ 0 &= -M_2 \omega^2 v_2 + C_1(v_2 - v_1) + C_2[v_2 - v_1 \exp\{ika\}] \end{aligned} \quad (10)$$

These equations for v_1 and v_2 can be solved non-trivially if the determinant vanishes [4] resulting in

$$\omega^2(k) = \frac{2C_x}{\gamma M_x} \left[1 \pm \sqrt{1 - \gamma^2 \frac{1 - \cos(ka)}{2}} \right] \quad (11)$$

with $\gamma = \frac{C_x M_x}{C_+ M_+} \leq 1$, where we have used the substitutions $X_+ = (X_1 + X_2)/2$, $X_x = \sqrt{X_1 X_2}$ for arithmetic and geometric mean respectively.

The dispersion relation from equation (11) has two branches as depicted in figure 4: (i) lower branch related to the acoustic mode (- sign) where neighboring atoms have similar phase (ii) upper branch related to optical mode (+ sign) where neighboring atoms have opposite phase.

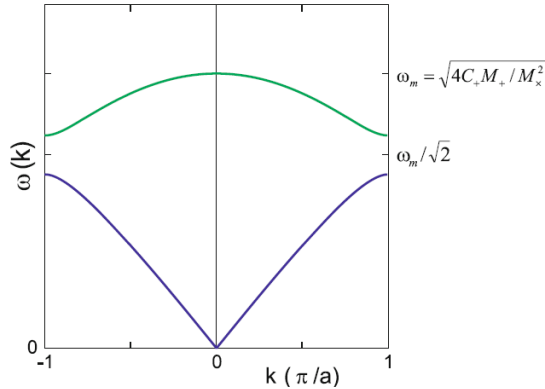


Figure 4: Dispersion relation of diatomic linear chain with acoustic (blue) and optical (green) branch [4]

We notice for the acoustic mode that $\omega = 0$ at the Γ point and increases towards the first Brillouin Zone (BLZ) boundary. The dispersion of the optical mode on the other hand is parabolic near the *Gamma* point with a negative curvature.

Due to opposite phases of oscillation between neighbors in the optical branch, a dipole moment may be created if atoms 1 and 2 have significant difference in electronegativity. Considering the excitation of these lattice oscillations (we will refer to quanta of lattice vibration as the quasi-particle phonon) by electromagnetic waves, energy and momentum conservation must be taken into account. At the edge of first BLZ, phonon wave vector is given by $k = \pi/a$, where a typical lattice constant of $a = 0.5$ nm can be considered. Most solids have energy width of the optical branch in some μm (meV). Thus, the ratio of phonon to photon momenta will be

$$\frac{p_{phon}}{p_{phot}} = \frac{\hbar k}{h/\lambda} = \frac{\lambda}{a} \approx \frac{\mu\text{m}}{\text{nm}} = 10^3 \quad (12)$$

with photon wave vector being several orders of magnitude lower than those of the phonons at the BLZ edge. We will thus only consider excitations of phonons near the Γ point.

1.3 Optical Response of Bound Charges: Lorentz Oscillator

We now extend equation (9) to study the influence of an external electromagnetic field $E_0 e^{i\omega t}$. Letting q_i be the electric charge of each atom,

$$\begin{aligned} M_1 \ddot{u}_n^1 &= -C_1(u_n^1 - u_n^2) - M_1 \eta v_n^1 - q_1 E_0 e^{i\omega t} \\ M_2 \ddot{u}_n^2 &= -C_1(u_n^2 - u_n^1) - M_2 \eta v_n^2 - q_2 E_0 e^{i\omega t} \end{aligned} \quad (13)$$

where the damping term η describes the decay of the oscillations after electric field switch-off as described in Figure 1. Setting $q_1 = -q_2 = -e$, the difference in the two equations yields

$$\ddot{u} = -\frac{C}{\mu} u - \eta v + \frac{eE_0}{\mu} e^{i\omega t} \quad (14)$$

with $u \equiv u_1 - u_2$ and $\mu = M_1 M_2 / (M_1 + M_2)$. With ansatz $u = u_0 e^{i\omega t}$, we get

$$u = \frac{eE_0}{\mu} \frac{1}{\omega_0^2 - \omega^2 - i\eta\omega} \quad (15)$$

where $\omega_0 = \sqrt{C/\mu}$ is the resonant frequency. The resulting polarization is

$$P_l = Ne(u_1 - u_2) = Neu \quad (16)$$

with N being the number of ion pairs per unit volume. From equation (2),

$$\chi^L = \frac{P}{\varepsilon_0 E} = \frac{A^2}{\omega_0^2 - \omega^2 - i\eta\omega} \quad (17)$$

where $A^2 = \frac{Ne^2}{\mu\varepsilon_0}$ is a coefficient that quantifies the strength of interaction between field and phonons. For multiple infrared active lattice vibrations, the susceptibility has to be taken into account, i.e. $\chi^L = \sum_i \chi_i^L$.

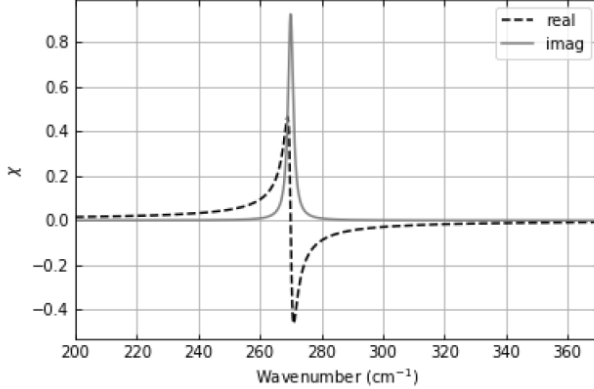


Figure 5: Real and imaginary part of lattice vibration susceptibility [6]

Depending on the direction of polarisation \mathbf{P} with respect to propagation direction \mathbf{k} we have two optical phonon modes: (i) $\mathbf{P} \parallel \mathbf{k}$, called longitudinal optical (LO) (ii) $\mathbf{P} \perp \mathbf{k}$, called transverse optical (TO) mode.

The LO and TO phonons shift charges in different ways and create different local polarisations. The LO phonon separates charges and creates internal electric fields that counteract the atomic displacements, thus requiring higher energy for LO-type atomic motion [3]. The difference due to $\omega_{LO} \geq \omega_{TO}$, also called LT splitting, gauges ionicity of the crystal. If LT split is much smaller than the attenuation, $A^2 \approx \omega_{LO}^2 - \omega_{TO}^2$ holds.

Assume an external field $\mathbf{E} = \mathbf{E}_0 e^{i(\mathbf{kr}-\omega t)}$ generates polarisation $\mathbf{P} = \mathbf{P}_0 e^{i(\mathbf{kr}-\omega t)}$ and displacement field $\mathbf{D} = \mathbf{D}_0 e^{i(\mathbf{kr}-\omega t)}$. From Maxwell's equations,

$$\nabla \cdot \mathbf{D} = 0 \text{ and } \nabla \times \mathbf{E} = 0 \implies \mathbf{k} \cdot \mathbf{D} = 0 \text{ and } \mathbf{k} \times \mathbf{E} = 0 \quad (18)$$

from which former conditions require that $\mathbf{D} = 0$ or $\mathbf{k} \perp \mathbf{D}$ (and therefore $\mathbf{k} \perp \mathbf{E}$), while the later condition requires $\mathbf{E} = 0$ or $\mathbf{k} \parallel \mathbf{E}$ (therefore $\mathbf{k} \parallel \mathbf{D}$). For the TO phonon, $\mathbf{D} \perp \mathbf{k}$, so \mathbf{E} is zero for the second condition to be fulfilled. Hence, $\varepsilon(\omega) \rightarrow \infty$ at ω_{TO} . On the other hand, LO phonon implies $\mathbf{E} \parallel \mathbf{k}$, so \mathbf{D} must be zero, which is only possible at $\varepsilon = 0$. Hence, a zero crossing of $\varepsilon(\omega)$ is expected at ω_{LO} . A schematic of $\varepsilon(\omega)$ obtained via the Clausius-Mosotti relation is depicted below:

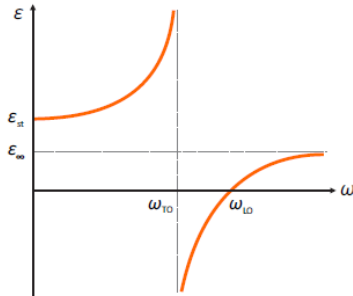


Figure 6: Schematic of $\varepsilon(\omega)$ due to interaction of optical phonon with light [3]

Note on IR active phonon modes: Every phonon mode of a non-cubic crystal does **not** show up in $\varepsilon(\omega)$ and IR spectrum. A coupling between light and phonon mode does not occur if no dipole is generated, which may be a common occurrence in covalent crystals or when phonon preserves inversion symmetry (leads to cancellation of all dipole moments). If a dipole moment parallel to \mathbf{E} is created, its coupling to the oscillating electric field renders the phonon mode IR-active [3].

1.4 Effects of Free Charge Carriers

In the previous section we discussed electrons constrained to harmonic motion around a fixed lattice site. For semiconductors however, electrons in the conduction band and holes in the valence band do not assume a fixed rest position and can generate electrical current. The presence of charge carriers can modify the dielectric function, thus affecting a material's electronic and optical properties.

A solution to the Schrödinger equation for the time evolution of a particle under the influence of an electric potential, as long as this is weak (so that no carriers are excited from one band to another) and does not change rapidly in time (so that the lattice may be regarded as continuous), is given by the effective mass approximation [5], i.e., the net effect of the periodic potential on the single electron inside the crystal changes the particle's mass from the value in free space to the effective mass m^* . The effective mass approximation allows us to write the equation of motion as:

$$m^* \ddot{x} + m^* \gamma_e \dot{x} = -eF \quad (19)$$

Here, x is the (simplified to 1D for symmetry arguments) position of the atom, γ_e represents a damping constant, and F represents the electric field strength, such that: $F = E_0 e^{i\omega t}$. Setting $\ddot{x} = 0$, we can define a **drift velocity** v_d :

$$\dot{x} = v_d = \frac{-e}{m^* \gamma_e} E_0 e^{i\omega t} \quad (20)$$

We characterize how quickly an electron or a hole can move through a metal or semiconductor when acted upon by an external electric field with **carrier mobility** μ defined by:

$$v_d = \mu E_0 e^{-i\omega t} \quad (21)$$

We can rewrite equation (20) to obtain a relation between damping and relaxation time τ to equilibrium state:

$$\gamma_e = \frac{-e}{m^* \mu} = \frac{1}{\tau} \quad (22)$$

Equation (19) is considered quasi-classical because it has been derived quantum mechanically (effective mass approximation), but once established, it can be classically determined using the ansatz for a harmonic oscillator:

$$x(t) = \frac{eE_0}{m^*} \frac{1}{\omega^2 + i\omega\gamma_e} e^{i\omega t} \quad (23)$$

Utilising the displacement x to obtain polarisation as done in (16),

$$P = \left(\frac{-Ne^2}{m^*(\omega^2 + i\omega\gamma_e)} \right) E_0 \quad (24)$$

Using the relation (2), we find the free charge carrier contribution to susceptibility,

$$\chi^P = \frac{-\omega_p^2}{\omega^2 + i\omega\gamma_e} \quad (25)$$

where ω_p is the plasma frequency, defined by the concentration of free charge carriers n_s :

$$\omega_p = e\sqrt{\frac{n_s}{\varepsilon_0 m^*}} \quad (26)$$

1.5 Complex Refractive Index & Absorption

The optical properties of a material can also be characterized by the complex refractive index and absorption coefficient. The **complex refractive index**: $\tilde{n} = n + i\kappa$, where n is the real part and κ the imaginary part, also called **extinction coefficient**.

In terms of the dielectric permittivity, it is related to \tilde{n} by $\varepsilon = \tilde{n}^2$, which leads to:

$$\varepsilon = \varepsilon_1 + i\varepsilon_2 \quad (27)$$

With:

$$\begin{aligned} \varepsilon_1 &= n^2 - \kappa^2 \\ \varepsilon_2 &= 2n\kappa \end{aligned} \quad (28)$$

The **absorption coefficient** α on the other hand describes the loss of intensity of light passing through a medium from a point r_1 to another point r_2 :

$$I(r_2) = I(r_1)\exp(-\alpha|r_2 - r_1|) \quad (29)$$

α is related to the imaginary part of refractive index by:

$$\alpha = \frac{2\omega}{c_0}\kappa \quad (30)$$

with c_0 being the speed of light in vacuum. As mentioned in section 1.1, it is now clear that the real part of the refractive index describes refraction, namely the change in speed of light inside the material, whereas the imaginary part describes absorption, that is the attenuation of the wave amplitude inside the material.

Absorption measurements require a suitably chosen sample thickness, such that the fraction of the absorbed intensity is neither too large nor too small. [3]. For that reason, it is often more convenient to measure **reflectance**, defined as the ratio of intensities of the incident and reflected light and better derived in the next section.

1.6 Reflectance and Transmittance

When an electromagnetic wave is incident on an interface, reflection and transmission occur. The ratio between the reflected (E_r) and transmitted (E_t) field strength to the incident (E_i) are called the reflection (r) and transmission coefficient (t) respectively. If we are dealing with plane waves incident normally to the surface (propagating in the z-direction):

$$\begin{aligned}\text{Incident: } E_i &= E_{i0}e^{i(k_0z-\omega t)} \\ \text{Transmitted: } E_t &= E_{t0}e^{i(nk_0z-\omega t)} \\ \text{Reflected: } E_r &= E_{r0}e^{i(-k_0z-\omega t)}\end{aligned}$$

At $z = 0$, the tangential component of electric field be continuous, thereby requiring: $E_{t0} = E_{i0} + E_{r0}$. A similar condition should hold for the magnetic field too. Therefore,

$$nE_{t0} = E_{i0} - E_{r0} \quad (31)$$

It is then trivial to obtain the reflection and transmission coefficients.

$$r = \frac{E_r}{E_i} = \frac{n_1 - n_2}{n_1 + n_2} \quad (32)$$

$$t = \frac{E_t}{E_i} = \frac{2n_1}{n_1 + n_2} \quad (33)$$

where n_1 and n_2 are the refractive indices of the incident and transmitted media respectively. This holds true only for an incident angle $\theta = 90^\circ$ for which Fresnel equations simplify considerably.

As the reflected and incident waves propagate in the same medium, they make the same angle with the normal to the surface. Hence, the **reflectance** R (or power reflection coefficient) is just,

$$R = |r|^2 \quad (34)$$

If we consider a material with non-negligible absorption (as such with a non-zero extinction coefficient κ), \tilde{n} has to be taken into consideration, and for a semi-infinite isotropic medium in vacuum (such that $n_2 = 1$):

$$R = \left| \frac{\tilde{n} - 1}{\tilde{n} + 1} \right|^2 \quad (35)$$

Equation 35 will be prominently made us of in this report, as we try to approximate vacuum conditions with normalization of our sample reflectance to a gold foil, which reflects around 97% of all light.

On the other hand, calculation of the transmittance (power transmission coefficient), is less straightforward since the light travels in different directions in the two materials and with a difference impedance. This results in:

$$T = \frac{n_2 \cos \theta_t}{n_1 \cos \theta_i} |t|^2 \quad (36)$$

Considering the normal incidence $\theta_i = \theta_t = 90^\circ$:

$$T = \frac{n_2}{n_1} |t|^2 \quad (37)$$

In conclusion: reflectance is the amount of flux reflected by a surface, normalized by the amount of flux incident on it. Transmittance is the amount of flux transmitted by a surface, normalized by the amount of flux incident on it.

Any flux not reflected or transmitted is absorbed. Hence conservation of energy requires:

$$R + T + A = 1 \quad (38)$$

In the context of the different structure of solids, electromagnetic waves incident on surfaces go through multiple successive reflections and transmissions. Thus, constructive and destructive interference of all rays will determine reflected and transmitted intensity.

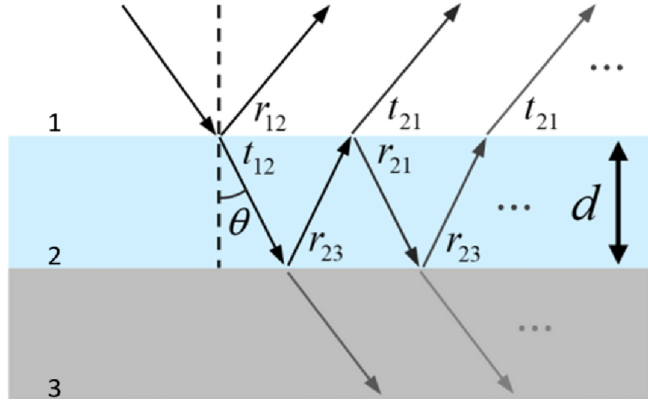


Figure 7: Wave propagation through stacked media [7]

The following are calculations in reference to Figure 7, assuming that incident waves are infinitely transmitted and refracted at both interfaces.

Let r_{mn} and t_{mn} be the reflection and transmission coefficient for an interface between material m and n , with d being the distance between the two interfaces. The total reflected field strength in multiple layers is:

$$E_r = r_{12}E_i \quad (39)$$

$$+ t_{12}r_{23}t_{21}e^{2ik_2d\cos\beta}E_i \quad (40)$$

$$+ t_{12}r_{23}r_{21}r_{23}t_{21}e^{4ik_2d\cos\beta}E_i \quad (41)$$

$$+ t_{12}r_{23}r_{21}^2r_{23}^2t_{21}e^{6ik_2d\cos\beta}E_i \quad (42)$$

$$+ t_{12}r_{23}r_{21}^3r_{23}^3t_{21}e^{8ik_2d\cos\beta}E_i \quad (43)$$

$$+ \dots \quad (44)$$

β is the propagation angle with respect to the normal surface, and $k_2 = \frac{2\pi n_2}{\lambda}$. The term in Equation (44) can be rewritten as:

$$E_r = \left(r_{12} + t_{21}t_{12}r_{23} \sum_{j=1}^{\infty} (r_{21}r_{23})^{j-1} e^{i2jk_2d\cos\beta} \right) E_i \quad (45)$$

In the above equation, the summation represents a geometric series: $\sum_{i=1}^{\infty} x^i = \frac{1}{1-x}$. Thus,

$$r = \frac{E_r}{E_0} = r_{12} + \frac{t_{21}t_{12}r_{23}e^{2ik_2d\cos\beta}}{1 - r_{21}r_{23}e^{2ik_2d\cos\beta}} \quad (46)$$

In the case of normal incidence ($\beta = 0$), $r_{mn} = -r_{nm}$ and $1 + r_{mn} = t_{mn}$ holds, and (46) simplifies to:

$$r = \frac{r_{12} + r_{23}e^{2ik_2d}}{1 + r_{12}r_{23}e^{2ik_2d}} \quad (47)$$

The reflectance is then:

$$R = |r|^2 = \frac{r_{12}^2 + r_{23}^2 + 2r_{12}r_{23}\cos k_2 d}{1 + r_{12}^2r_{23}^2 + 2r_{12}r_{23}\cos k_2 d} \quad (48)$$

For a sufficiently narrow spectral bandwidth (ensures that interference effects remain coherent) and negligible absorption loss $\kappa < 0.1n$, sample thickness d can be calculated by measuring distance between two neighboring interference maximas,

$$d = \frac{N_1 - N_2}{2n(\tilde{\nu}_1 - \tilde{\nu}_2)} \quad (49)$$

where N is the order of the maximas and $\tilde{\nu}$ the wavenumber.

1.7 Fourier Transform Infrared Spectroscopy (FTIR)

FTIR is based on the idea of the interference of radiation between two beams to yield an *interferogram*. The latter is a signal produced as a function of the change of path length between the two beams. Fourier-transformation is used to achieve the inter-convertibility between the distance and frequency domain [8].

The key components of a typical FTIR spectrometer is shown schematically in Figure 8.



Figure 8: Schematic of typical FTIR components [8]

Same types of radiation sources are used for both dispersive and FTIR spectrometers, however it is more often water cooled in FTIR systems for better power and stability [9]. Typically, an inert solid such as Nernst glower, Globar, or Nichrome coil is electrically heated to 1000 to 1800°C.

The interferometer replaces the monochromator which is used in traditional dispersive spectrometers. The most commonly used type is a Michelson interferometer which consists of a beamsplitter (semireflecting device often made of Ge thin film on KBr substrate) to split the IR beam and a moving mirror that creates varying path lengths between them.

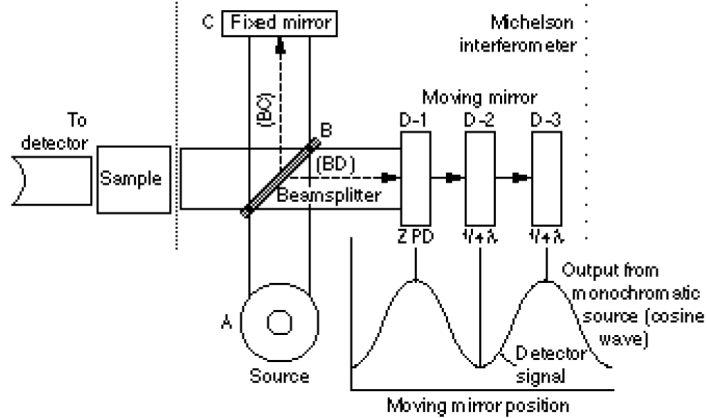


Figure 9: Simplified optical layout of typical FTIR [9]

As shown in Figure 9, the interferometer generates an interference pattern by varying the optical path difference between the beams reflected off the fixed and moving mirrors. As the moving mirror changes position, the recombined beams produce a series of constructive and destructive interferences, creating the interferogram. This interferogram contains information about all the IR frequencies simultaneously. The distance D-1 of the moving mirror in Figure 9 depicts the zero path difference (ZPD) where the two beams are in-phase. Assuming monochromatic source, when the mirror is moved at a *constant velocity*, the intensity of radiation reaching the detector varies in a sinusoidal manner and is recorded as a time domain interferogram. If significant absorption takes place within the sample, the amplitude of the sinusoidal wave is reduced by an amount proportional to amount of sample in the beam [9]. For a polychromatic source the interferogram will take the form as shown below:

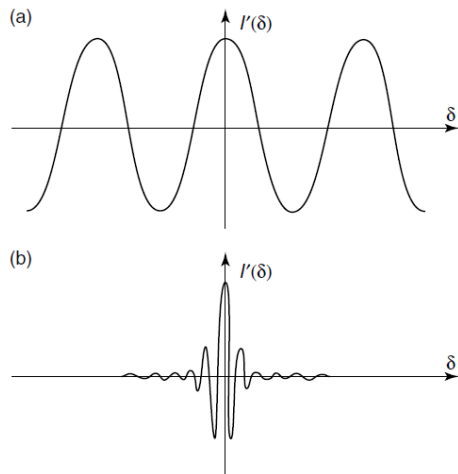


Figure 10: Interferogram obtained from (a) monochromatic radiation (b) polychromatic radiation [8]

The equations for a Fourier-transformation relating intensity $I(\delta)$ falling on the detector as function of path length δ to the spectral power density $B(\bar{\nu})$ for a particular wavenumber $\bar{\nu}$ are:

$$\begin{aligned} I(\delta) &= \int_0^{+\infty} B(\bar{\nu}) \cos(2\pi\bar{\nu}\delta) d\bar{\nu} \\ B(\bar{\nu}) &= \int_{-\infty}^{+\infty} I(\delta) \cos(2\pi\bar{\nu}\delta) d\delta \end{aligned} \quad (50)$$

which together form a Fourier-transform pair.

The interferogram is an analogue signal at the detector that has to be digitalized such that a Fourier transform can be performed. In order to minimize error the following considerations are made:

1. Zero Padding: Signal resolution is enhanced prior to applying a Fourier transform by adding trailing zeros. This increases the length of a FFT result vector which in turn has more frequency bins. Ultimately, it results in a smoother looking spectrum.
2. Apodization: Mathematical FT assumes infinite boundaries. However, the transformation carried out in practice involves an integration stage carried out over a finite displacement. The line shape of a transformation may contain series of side lobes (or pods) near the main band. If these lobes are large, the obtained spectrum will contain irregularities analogous to peaks.

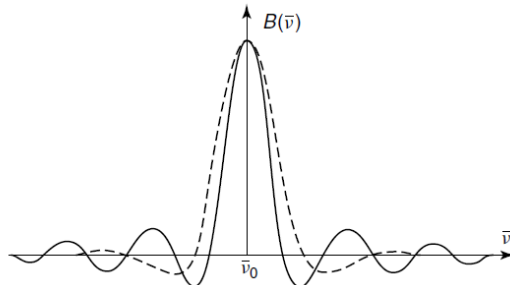


Figure 11: Instrument line shape without apodization [8]

The apodization process removes these lobes by multiplying the interferogram by a suitable function prior to FT. The cosine function $F(D) = [1 + \cos(\pi D)]/2$ can serve as a general purpose apodization function, although most softwares will offer a range of choices.

3. Phase Correction: If the sample intervals are not exactly the same on either side of a maxima corresponding to ZPDs, a phase correction will be required. We need to ensure that sample intervals are equal on either side of the first interval corresponding to a path difference of zero. A software will automatically apply a phase correction factor to align spectral peaks.

1.8 Spectral Analysis

In an infrared spectrum, the ordinate scale may be representative of either absorbance or transmittance as a measure of band intensity. The relationship

between these two quantities has been explored in 1.6. The transmittance spectra provides better contrast between strong and weak lines and has been traditionally used for spectral interpretation, while absorbance is used for quantitative work.

The mid-infrared spectrum ($4000 - 400\text{cm}^{-1}$) can be further divided into four regions, and the effect of an absorption or transmission phenomena may be determined by the region in which it is located. Transitions between vibrational energy states may be induced by absorption of photons of the appropriate energy. It requires more energy to stretch (or compress) a bond than to bend it, and the energy (or frequency) that characterizes the stretching vibration of a given bond is proportional to the bond dissociation energy. These regions are the following:

- Hydrogen bonds X–H stretching region ($4000 - 2500\text{cm}^{-1}$): Here we usually see O–H (3700–3600), C–H (3000–2850) and N–H (3400 and 3300) stretching.
- Triple-bond stretching region ($2500 - 2000\text{cm}^{-1}$): The most common absorptions in this region are due to $C \equiv C$ bonds, absorbing between 2300 and 2050 with a very weak stretching, and the nitrile group ($C \equiv N$), occurring between 2300 and 2200 and present more moderate stretching. However X–H stretching absorptions with more massive X atom such as phosphorus or silicon also occur at these frequencies.
- Double bond region ($2000 - 1500\text{cm}^{-1}$): The principal absorption in this region are due to C=C and C=O stretching, with carbonyl stretching (C=O) being usually the most intense line in the spectrum. C=N stretching also occurs in this region and is usually moderately strong.
- Fingerprint region ($1500 - 600\text{cm}^{-1}$): Many vibrations are not so well behaved as the previously listed bonds stretching, even for similar molecules. This applies to most absorption in the 1500–650 region, where electronic effects (previously covered) lead to large shifts. This entails that a spectrum may have a hundred or more absorption bands with the majority of them being nonassignable (and with no need to do so)

For even lower $\tilde{\nu}$, the far-infrared region is defined in $400 - 100\text{cm}^{-1}$. Here there is less spectra–structure correlations, but does provide information regarding the vibrations of molecules containing heavy atoms, molecular skeleton vibrations, molecular torsions and crystal lattice vibrations. Intramolecular stretching modes involving heavy atoms can be helpful for characterizing compounds containing halogen atoms, organometallic compounds and inorganic compounds [8].

2 Experimental Setup

This lab utilizes the PerkinElmer Spectrum Two FT-IR spectrometer [11]. The experimental setup is depicted below:



Figure 12: Experimental setup for FTIR spectroscopy [10]

SpectrumTM software was used to record the spectrometer data that has in-built error mitigation algorithms as mentioned in Section 1.7. The components of the spectrometer is depicted below:

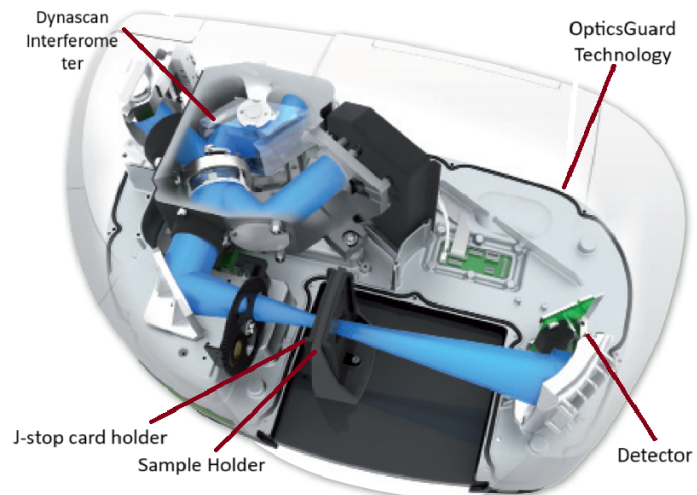


Figure 13: 3D render of the Spectrum Two spectrometer [11]

Spectrum Two uses a room-temperature LiTaO₃ detector with a signal-noise-

ratio (SNR) of 9300:1. The spectral range is $8300 - 350\text{ cm}^{-1}$ with maximum resolution of 0.5 cm^{-1} . An inherent flaw of the interferometer mentioned in 1.7 is that the moving mirrors can undergo tilt and shear which is a result of misalignment. This introduces random noise and also affect intensity at the detector. The Dynascan interferometer utilizes a rotating pivoting mirror pair, which prevents misalignment and making our spectrometer immune to tilt and shear. In the digitization of the FT-IR interferogram, use of Sigma-Delta converters enhances the dynamic range, reduces spectral artifacts, and increases ordinate linearity [11].

3 Results & Discussion

3.1 Task 1: Calibration of the wave-number scale

The first task consists of verifying instrument calibration. To that end, we first measure the transmittance spectra with an empty sample holder, and then using a polystyrene foil sample. Recording the transmittance spectra of air has a second purpose, as we will additionally use it throughout the report to normalize the rest of our spectra.

3.1.1 Water vapor

As approximately 1% of air is water vapour, the recorded spectra should show known absorption lines of water at specific spectral positions. Reflection and absorption from other molecules present in air also takes place, thereby increasing the noise considerably. However, we aim to confirm the position of only the specifically selected water vapor calibration lines, and compare them to theory.

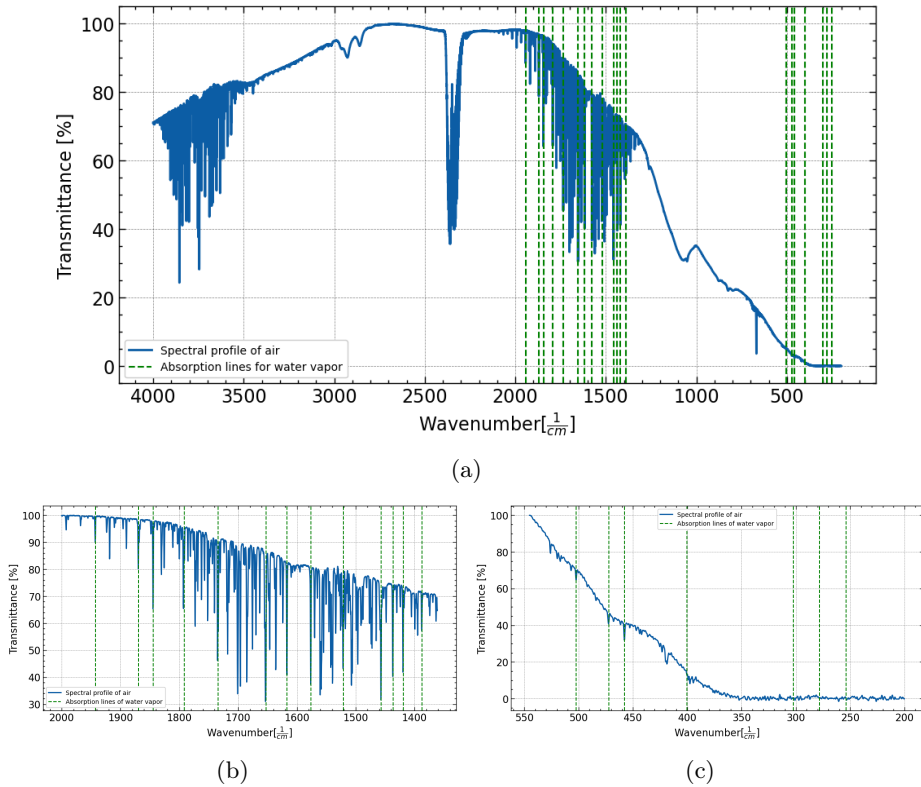


Figure 14: Transmission spectrum of empty sample holder with water vapor lines in (a) the entire measured range (b) the high and (c) low wave-number range

Note that the y-axes of the graphs were normalized such that the highest intensity value was set to represent 100% transmittance. The measurements

were taken with a resolution of 1cm^{-1} , due to which we assign a systematic error of $\epsilon = \pm 0.5\text{cm}^{-1}$.

The experimentally recorded position of each line is then manually recorded and compared to theory (from table in [6]). We then assign a deviation Δd defined as the difference between the experimental and theoretical wave-number of each line. Note that the associated error ϵ for the experimental value contributes to Δd as well.

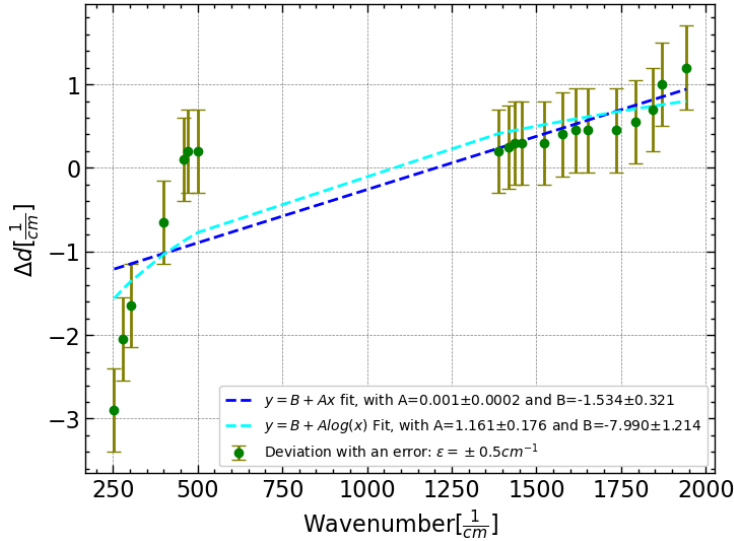


Figure 15: Deviation of water vapor’s transmission lines with respect to wavenumber

Applying a linear fit to the deviations provides insights into the systematic biases of our spectrometer. A non-zero slope $A = 0.001 \pm 0.0002$ indicates a dependence (even though very small) of Δd on wavenumber. We note that $\Delta d < 0$ for wavenumbers up to around 500cm^{-1} and $\Delta d > 0$ for higher values. This infers an optimum central wavenumber $\tilde{\nu}_0$ with null deviation,

$$\tilde{\nu}_0 = \frac{-B}{A} \pm \tilde{\nu}_0 \sqrt{\left(\frac{\delta B}{B}\right)^2 + \left(\frac{\delta A}{A}\right)^2} \implies \tilde{\nu}_0 = 1534 \pm 444 \text{ cm}^{-1} \quad (51)$$

The spectrometer has optimized accuracy around this $\tilde{\nu}_0$. This may be due to combined effects of dispersion characteristics of optical components, alignment, and possibly thermal effects. A logarithmic fit is included for visualization purposes only and is not utilized in the analysis.

3.1.2 Polystyrene foil

We repeated the same process with a polystyrene foil, using the water vapor spectrum as our normalization reference. This allows us to eliminate some of the noise due to external molecules. This is noticeable in Figure 16 (a) around $\tilde{\nu} \approx 2300\text{cm}^{-1}$, where we see intense lines, which do not seem to match with our theoretical models of Polystyrene. Upon normalization with water vapour

in (b), the discrepancies disappear. Note that sample imperfections and other systematic factors still contribute to the noise.

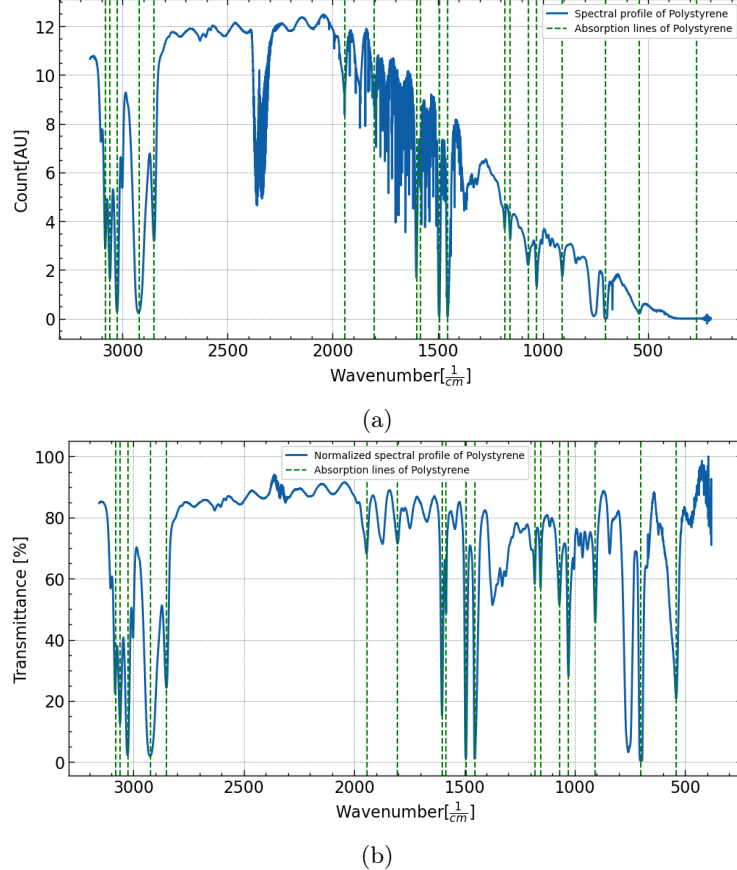


Figure 16: Transmission spectra for Polystyrene (a) without normalization and (b) with normalization to water vapour, with dashed calibration lines

The behavior of deviation between the experimental position of our peaks and the theoretical values given in [6] can once again be evaluated.

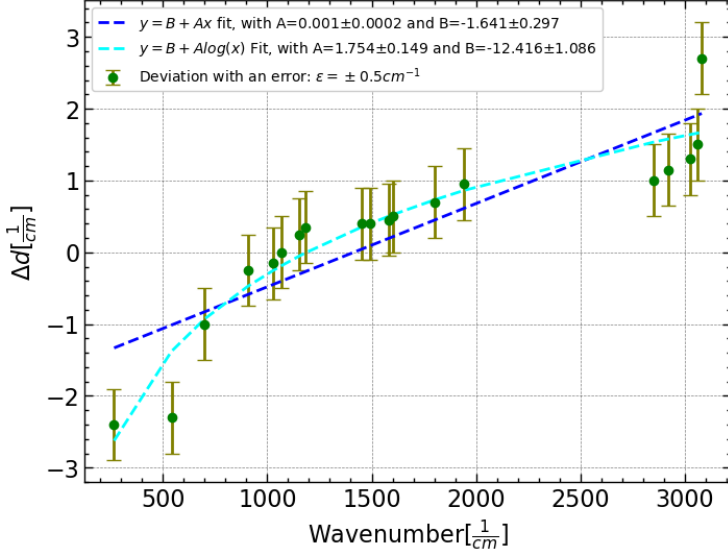


Figure 17: Deviation of Polystyrene’s transmission lines with respect to wavenumber

Like water vapour, polystyrene also presents a central $\tilde{\nu}_0$ for which Δd is minimal. Here,

$$\tilde{\nu}_0 = 1641 \pm 443 \text{ cm}^{-1} \quad (52)$$

Both samples yield the same wavenumber dependence A from the linear fit of Δd . In order to obtain a wavenumber calibration for the rest of the report, we will take a weighted average of water vapor and polystyrene deviation fits in the form,

$$\bar{x} = \frac{\sum_i w_i x_i}{\sum_i w_i} \quad (53)$$

where $w_i = \frac{1}{\delta_i^2}$ with δ_i being the corresponding uncertainty of measurement x_i . This yields,

$$\delta\tilde{\nu}_c = 0.001\tilde{\nu}_m - 1.5857 \quad (54)$$

where $\delta\tilde{\nu}_c$ is the calibrated offset of our wavenumbers, and $\tilde{\nu}_m$ the measured value. Wherever appropriate, we will calibrate the wavenumbers by

$$\tilde{\nu}_c = \tilde{\nu}_m + \delta\tilde{\nu}_c \quad (55)$$

3.2 Task 2: Glass and NaCl blocking filters

In this second task we look at the detected signal strength in the blocking ranges of Glass and NaCl blocking filter.

3.2.1 Glass

For the glass filter, we measure the following spectra.

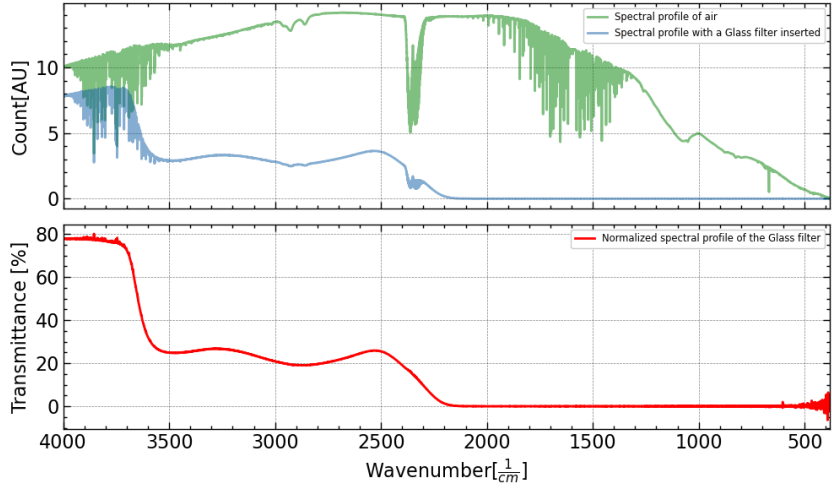


Figure 18: Normalized transmission spectra of air with (blue) and without (green) a glass filter inserted, and their ratio (red)

As expected, we notice an overall decrease in intensity at the detector from Figure 18. At high $\tilde{\nu}$ the filter allows for most light to pass, but present a sharp drop at $\tilde{\nu} \approx 3600 \text{ cm}^{-1}$ and a second one at $\tilde{\nu} \approx 2300 \text{ cm}^{-1}$.

The range $2200 \text{ cm}^{-1} \gtrsim \tilde{\nu} \gtrsim 500 \text{ cm}^{-1}$ is where the glass filter presents negligible transmittance, but its effectiveness wanes for even lower $\tilde{\nu}$. We can visualize this in the following figure:

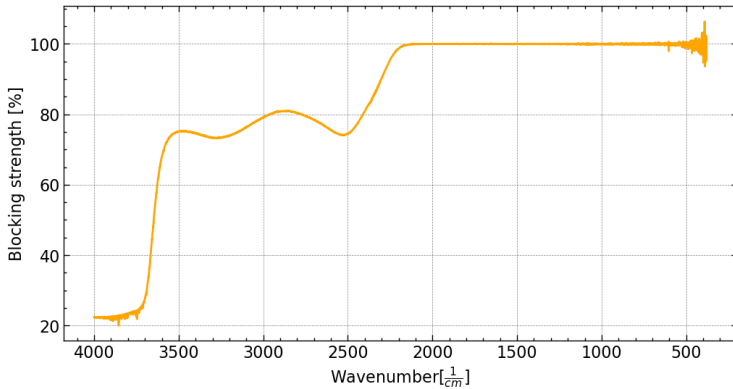


Figure 19: Blocking strength of glass filter with respect to $\tilde{\nu}$

Glass is typically transparent to IR radiation in the high wavenumber range (short wavelengths). As we are unaware of the exact chemical composition of the glass filter, certain predictions are made:

- $3500\text{-}2500 \text{ cm}^{-1}$: This range includes absorption due to hydroxyl (O-H) groups, which are commonly present in glass due to water content. They present a broad absorption with Figure 18 showing two convoluted peaks that may be due to asymmetric and symmetric O-H stretches [13].

- 2000-500 cm⁻¹: The strongest absorption bands in silicate glasses, such as soda-lime or borosilicate glass occur in this range. The stretching of Si-O-Si bonds in the silicate network occur around 1100-1000 cm⁻¹, and bending modes of Si-O bonds occurring around 450-500 cm⁻¹ [14]. Glass is an amorphous material, thereby lacking long range order. The complexity of a SiO₄ tetrahedra network also leads to numerous vibrational modes creating a continuous absorption over this broad range. Impurities and defects can also introduce additional vibrational states.

Further analysis is required for the lower range $\tilde{\nu} \approx 250\text{cm}^{-1}$. We noticed that spectral profile of air around 350 cm⁻¹ has values almost 1-2 orders of magnitude lower than polystyrene, sapphire, etc. with sometimes even being negative. This creates a shoot up upon normalization, making it appear disproportionately significant. We thus chose to neglect this region in the discussion.

3.2.2 NaCl

Similar analysis is performed for an NaCl filter and the following figure is obtained:

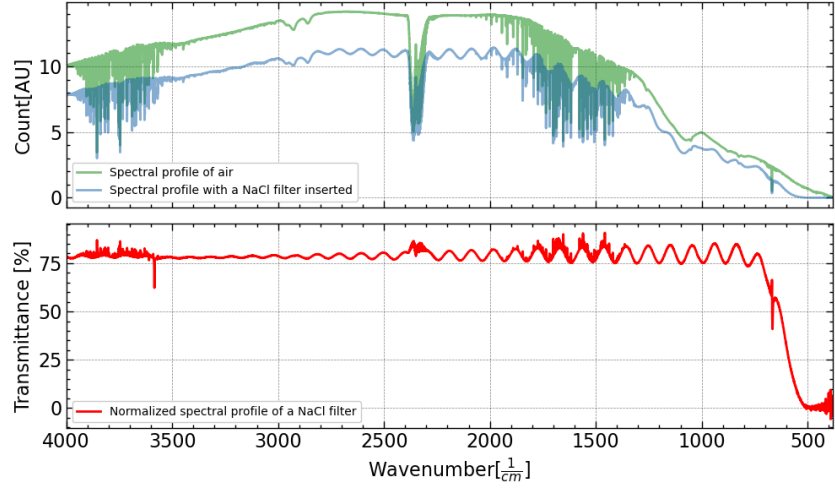


Figure 20: Transmission spectrum of air with (blue) and without (green) an NaCl filter inserted, and the normalized transmittance of NaCl(red)

This corresponds to a filtering that focuses almost entirely on low $\tilde{\nu} \lesssim 500\text{cm}^{-1}$:

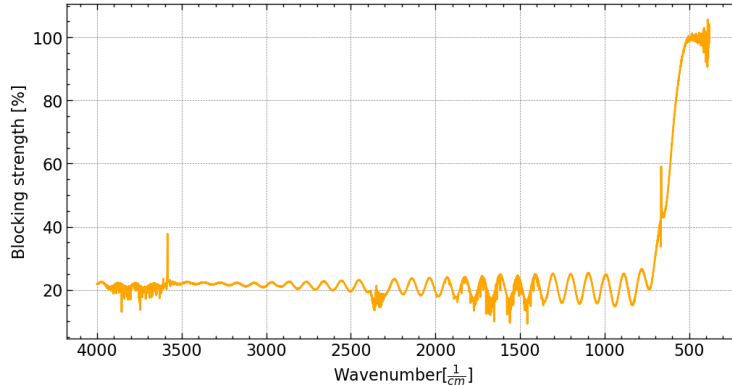


Figure 21: Blocking strength of NaCl filter with respect to light's \tilde{v}

NaCl filters (also called "salt plates") are often used in organic chemistry labs due to their transparency to IR radiation. In Figure 21, we see blocking of light only in the far-IR region. Typical absorbance occurs due to vibrations of atoms that participate in a functional group. Ionic bonds however, are electrostatic and they do not share the same orbital. In the mid-IR range, photons do not have sufficient energy to excite the fundamental phonon modes of the NaCl crystal, and hence presents a low blocking strength. From [15] (p. 280), NaCl phonon modes are $\tilde{\nu}_{\text{LO}} = 264 \text{ cm}^{-1}$ and $\tilde{\nu}_{\text{TO}} = 163 \text{ cm}^{-1}$ with 100% reflectivity in between due to the *Restrahlen effect*.

3.3 Task 3: Reflectivity and Transmission spectrum of Sapphire

We now measure the transmission and reflectivity spectrum of Al_2O_3 and determine characteristic quantities of the dielectric function such as energy of phonon modes, background dielectric constant ϵ_∞ , and damping constant.

3.3.1 Reflectivity Spectrum and Dielectric Function

So far we have only looked at the transmission spectrum of our samples, but a modification of our set up with a reflectance accessory allows us to determine the reflectivity as well. We use gold for normalization, which supposedly reflects around 97 % of incident light. Due to limitations of our instrument, the resolution of our measurements was increased to 4 cm^{-1} .

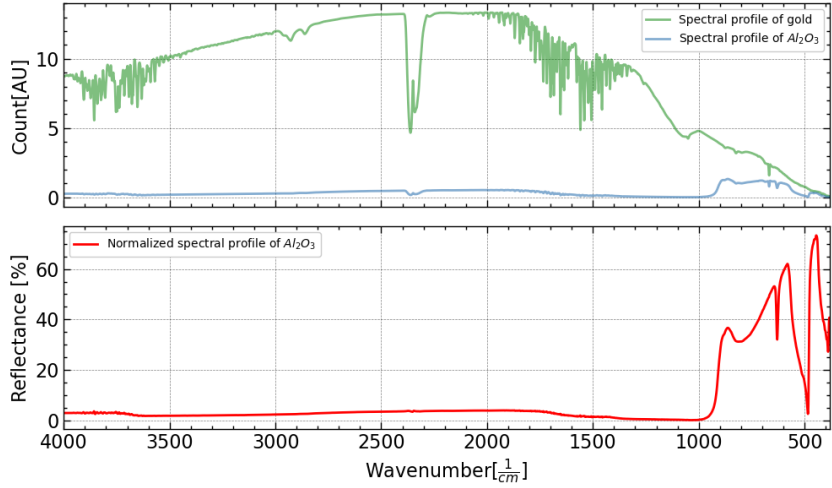


Figure 22: Reflectivity spectrum of gold (green), sapphire (blue), and the reflectance of sapphire normalized to gold(red)

The main contribution to the reflectance is from the fingerprint region of the spectrum, using which we now determine the dielectric function from equations (7) and (17). Additionally, equation (35) gives a relationship between the dielectric function ε and the reflectance R by the means of the refractive index n . Thus,

$$R = \left| \frac{1 - \sqrt{\varepsilon_\infty + \sum_i \chi_i^L}}{1 + \sqrt{\varepsilon_\infty + \sum_i \chi_i^L}} \right|^2 \quad (56)$$

Note that sapphire is an insulator with a band gap of around 9 eV, and even with various dopants, it is difficult to make it conductive. From figure 22 we can see 4 main peaks in the spectral profile of Al_2O_3 , as such we can imagine the presence of 4 different phonon mode contributions. We can fit this to our function, keeping in mind that the choice of initial parameters is very important. Each phonon contribution term χ_L will approximate one of the peaks, with A representing phonon-field coupling, ω_0 the resonance peak position, and η the phonon damping (also related to the peak width). Note that the fitting is highly dependent on initial guesses and a different method should be used for more accurate analysis.

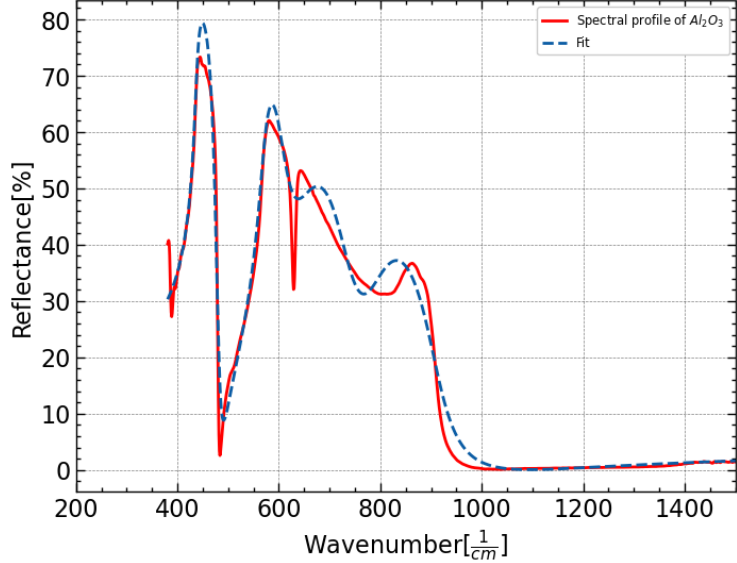


Figure 23: Reflectance spectrum of normalized sapphire in the far to mid IR region with fit

The fitting parameters we obtain are the following:

Parameters	Fitting values [cm^{-1}]
A_1	557.122 ± 1.867
ω_{01}	437.996 ± 0.209
η_1	10.445 ± 0.228
A_2	599.847 ± 4.647
ω_{02}	569.647 ± 0.330
η_2	26.418 ± 0.791
A_3	480.728 ± 10.337
ω_{03}	639.548 ± 1.219
η_3	106.401 ± 3.655
A_4	326.173 ± 5.887
ω_{04}	781.645 ± 0.995
η_4	118.927 ± 2.729
ε_∞	2.196 ± 0.009

Table 1: Table of fitting parameters

Calculated background dielectric $\varepsilon_\infty = 2.196 \pm 0.009$ was close to literature values of $\alpha\text{-Al}_2\text{O}_3$ as measured by Harman 1994 [18]. The obtained parameters from Table 1 allow us to apply equation (56) to plot the complex dielectric function:

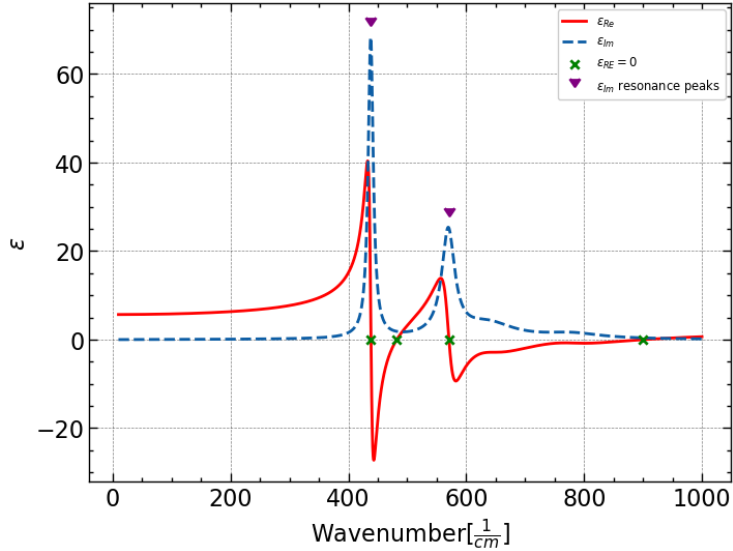


Figure 24: Dielectric function's real and imaginary part

The following table shows the values at which $\text{Re}(\varepsilon)=0$, and the resonance peak positions of $\text{Im}(\varepsilon)$:

Zero-crossing index	$\tilde{\nu}$ [cm^{-1}]	Resonance peaks index
1	438.484 ± 0.001	1
2	482.168 ± 0.001	—
3	570.797 ± 0.001	2
4	900.540 ± 0.001	—

Table 2: Zero-crossing of $\text{Re}(\varepsilon)$ and resonance peaks of $\text{Im}(\varepsilon)$

LO and TO phonons create different local polarizations. For LO phonons, the displacement of charges is parallel to the applied field. This separation of charges creates internal electric fields that counteract atomic displacements (also why higher energy is required for LO phonons) [3]. At $\text{Re}(\varepsilon_{LO})=0$ this internal field is maximized and we can identify the LO modes of sapphire from Table 2.

TO phonons on the other hand corresponds to strong absorption in the material due to resonance between the field and atomic oscillators. The resonance positions, and thus ε_{TO} can be seen from Table 2. All the obtained vibrational modes are displayed below:

Index (j)	$\tilde{\nu}_{LO}$ [cm^{-1}]	$\tilde{\nu}_{TO}$ [cm^{-1}]
1	438.484 ± 0.001	437.996 ± 0.209
2	482.168 ± 0.001	569.647 ± 0.330
3	570.797 ± 0.001	639.548 ± 1.219
4	900.540 ± 0.001	781.645 ± 0.995

Table 3: Derived vibrational modes of sapphire

Note that all the wavenumbers derived in this task were calibrated according to

equation (55). Irreducible representations (irreps) are group theoretical notations applied in crystallography used to describe symmetry properties of phonons. For an E_u modes, E denotes a two-fold degenerate vibration, while subscript u indicates odd parity (anti-symmetric with respect to inversion through the center of symmetry of the crystal). For A_{2u} modes, A denotes a non-degenerate vibration, while the subscript again assigns an odd parity.

The $j=2$ LO mode is an exact match to an E_u mode from Gervais et. al. IR-reflectivity (1974) [19]. The corresponding TO mode is also a very close match of another E_u mode. The $j=1$ TO mode has a relative uncertainty of 0.3% compared to one measured E_u by the same study. The LO phonon however, has an uncertainty of 13% when compared to the closest match. The $j=3$ TO presents an uncertainty of 0.7% with respect to an E_u mode literature value by Barker (1963) [20]. The LO phonon again, has an offset of $\pm 9\%$ depending on whether we compare it to an E_u or A_{2u} mode respectively. For $j=4$, LO presents a perfect match with an E_u mode while there was a lack of literature data in the 800 cm^{-1} range for the TO phonon. Most of the matches were thus E_u modes.

Single crystal of aluminium oxide, $\alpha\text{-Al}_2\text{O}_3$, has a stable corundum at high temperatures. The basis of the crystal are octahedrons with O^{2-} ions at the corners, and Al^{3+} ions in the center. It has a trigonal crystal structure (space group $\text{R}\bar{3}\text{c}$), but generally treated as a hexagonal crystal as shown in the below:

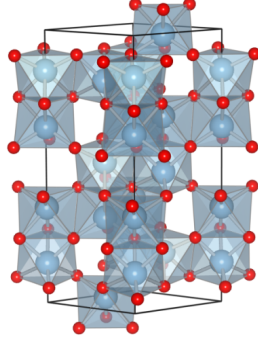


Figure 25: Corundum Structure of Sapphire (ICSD-10425; drawn using VESTA) [21]

The trigonal symmetry of sapphire allows for multiple E_u modes. They involve in-plane vibrations which are more likely to couple with IR radiation compared to A_{2u} modes, which involve c-axis vibrations. Schematic representation of LaAlO_3 modes that also presents $\text{R}\bar{3}\text{c}$ symmetry is shown below:

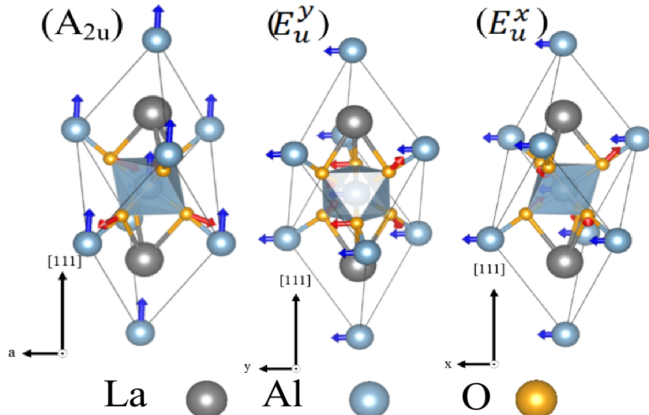


Figure 26: A_{2u} and E_u vibration modes of $R\bar{3}c$ space group [22]

Note that an $A^2 = \tilde{\nu}_{LO}^2 - \tilde{\nu}_{TO}^2$ fit was not performed as it significantly degraded the quality of the fit and introduced substantial errors.

3.3.2 Transmission Spectrum and sample thickness

Now we study the transmission spectrum of our sapphire sample and normalize it to air.

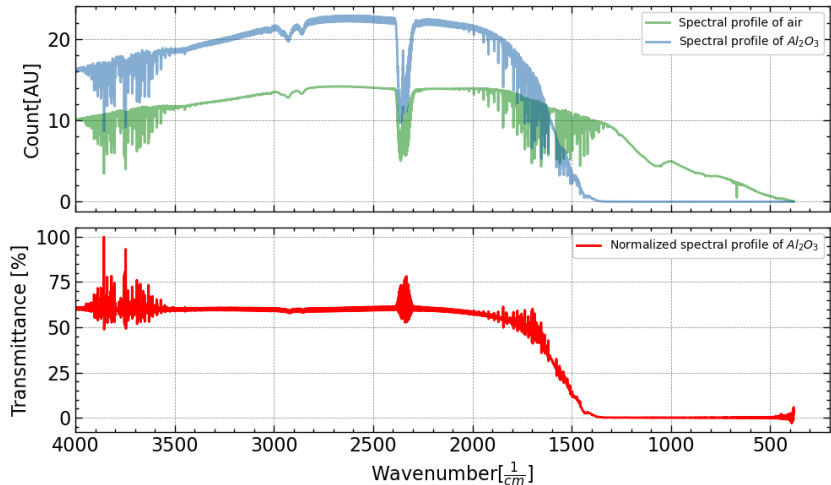


Figure 27: Transmission spectrum of air (green), sapphire (blue), and the transmittance of sapphire normalized to air(red)

Transmittance of sapphire is maximum around 55% in the 4000-2000 region, with peaks around 3800. Using equation (49) we can focus on one region of the spectrum with multiple peaks and estimate our sample thickness by the measured distance between two neighboring interference maximas. Note that wave-numbers have again been adjusted previous to our calculations based on 55. A best estimations for our distance requires sufficiently narrow and coherent spectral bandwidth. Two different ranges were chosen to favor these conditions

and subsequently averaged. For each subset the error is the standard error of the mean.

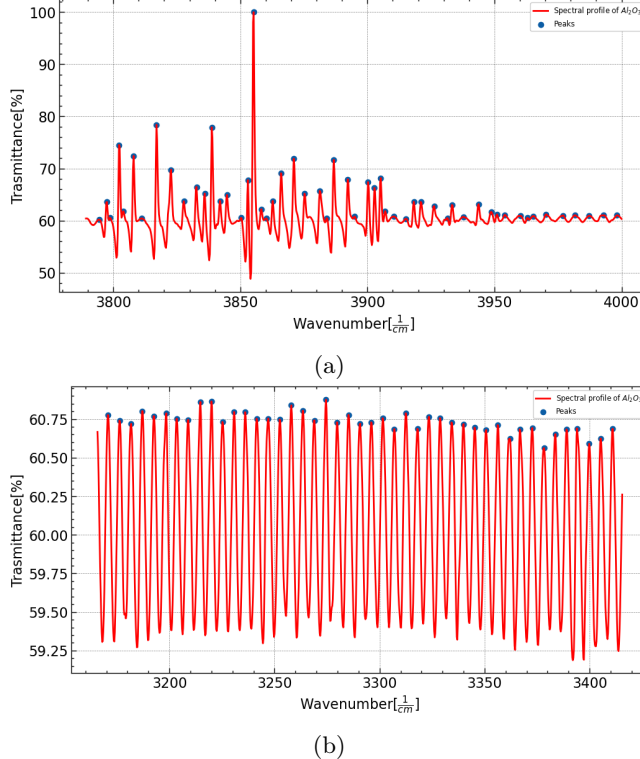


Figure 28: Normalized transmission spectrum of Sapphire in the (a) $3800 - 4000 \text{ cm}^{-1}$ and (b) $3200 - 3400 \text{ cm}^{-1}$ ranges, with marked peaks.

As we only analyze the neighboring maxima, the difference in the order of interference is $N_i - N_{i+1} = 1$ for all measurements. Since $\tilde{n} = \sqrt{\varepsilon}$, we are able to calculate the real refractive index from the previously obtained parameters by plotting the dielectric function over the whole spectra, such that: $n_a = 1.459 \pm 0.001$ and $n_b = 1.450 \pm 0.001$ (as an average of the chosen range) which then yields:

$$d_a = 0.0895 \pm 0.0016 \text{ cm}$$

$$d_b = 0.0896 \pm 0.0017 \text{ cm}$$

We can average them and conclude that the thickness of our sample is:

$$\bar{d} = (0.8928 \pm 0.0016) \text{ mm} \quad (57)$$

3.4 Task 4: Optical properties of Silicon

In this task our aim is to determine optical properties of Silicon by extracting information from its transmittance and reflectivity spectrum. For both scans, the resolution was kept at 4cm^{-1} .

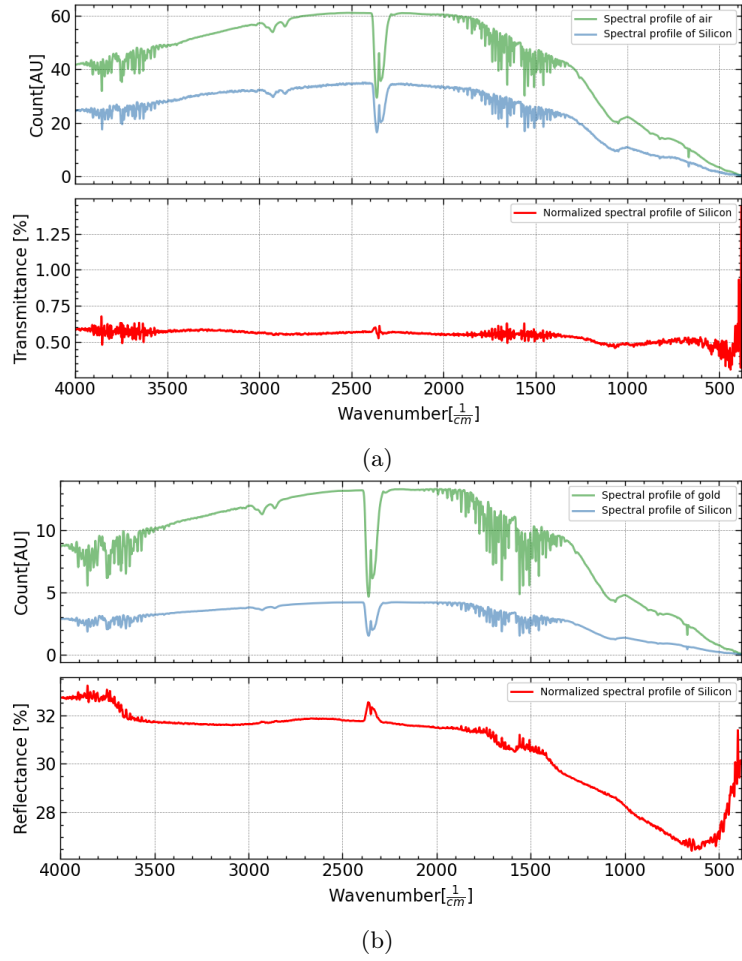


Figure 29: (a) Transmittance (due to extensive absorption, we have **multiplied the blue Si profile here by 100** for only visualization purposes) and (b) Reflectance of Silicon

3.4.1 Absorbance

Conservation of energy is such that $R + T + A = 100\%$. Using T and R from Figure 29, we can plot the Absorbance:

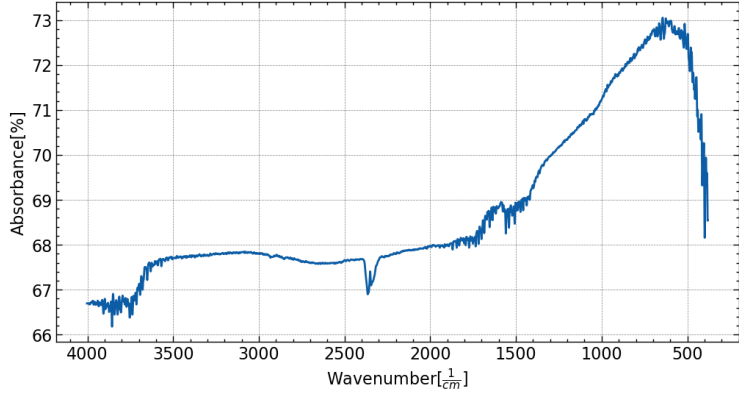


Figure 30: Absorbance of Silicon

We see that Silicon has high absorption in the entire mid IR region, and shows a sharp and steep decrease under $\tilde{\nu} = 400\text{cm}^{-1}$. A calculation of the absorption and extinction coefficients was thus deemed appropriate.

3.4.2 Absorption (α) and Extinction (κ) coefficients

As covered in Section 1.5, the absorption coefficient is directly proportional to the imaginary part of the refractive index, and quantifies the attenuation rate of a wave amplitude passing through a material. Prior to determining α , we need to calculate the sample thickness d by employing the same method used in the previous section.

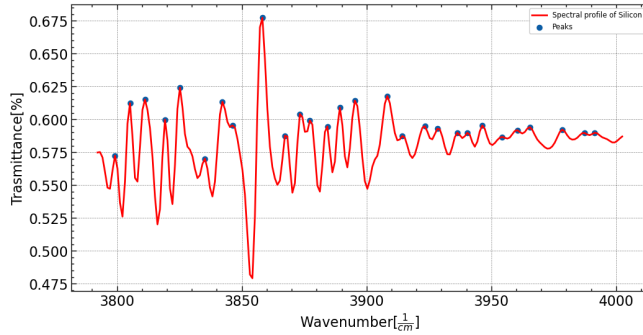


Figure 31: Interference peaks of Silicon transmittance spectrum in the 3800-4000 cm^{-1} region

After proper calibration and using equation (49), we find d to be, ($n=3.44$ at around $\tilde{\nu} = 4000\text{cm}^{-1}$ from [17]) :

$$d_{sili} = 0.020\text{cm} \pm 0.001\text{cm}$$

The relationship between Absorption and α can be obtained by accounting for an effective transmittance such that,

$$T_{\text{eff}} = \frac{T}{(1 - R)^2} \quad (58)$$

Applying this to equation (29) yields

$$\alpha = -\frac{1}{d} \ln \left(\frac{T}{(1-R)^2} \right) = \frac{1}{d} \ln \left(\frac{(1-R)^2}{T} \right) \quad (59)$$

The expression for T_{eff} accounts for a geometric series sum of multiple reflections at the air-film interface, and internal reflections [30]. Given this and equation (30), we can plot the two coefficients as functions of wavenumber:

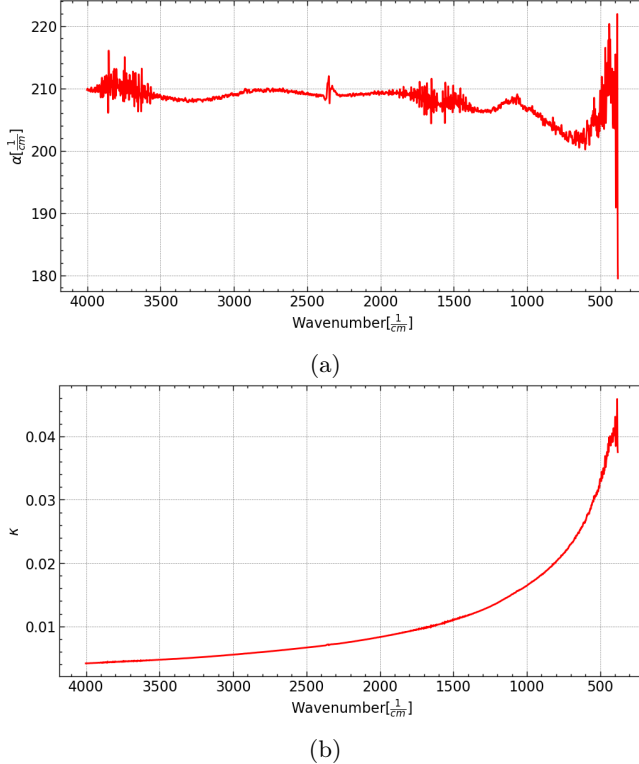


Figure 32: (a) Absorption coefficient α and (b) extinction coefficient κ of Silicon in the $4000 - 400 \text{ cm}^{-1}$ region

In the $4000-1500 \text{ cm}^{-1}$ range, κ is steadily increasing, possibly due to free charge carrier absorption. Phonon effects become dominant as wavenumber decreases to the 500 cm^{-1} range. The κ values can be verified from the database in [17] from Horowitz (2005). Silicon has optical phonon modes around 520 cm^{-1} , that contributes to increased absorption [31]. While silicon's bandgap of 1.1 eV corresponds to around 10000 cm^{-1} , far above the infrared range we are investigating, the indirect nature of the bandgap may allow for phonon-assisted interband transitions.

3.5 Task 5: Phonon properties of ZnO Thin Film

We now determine phonon properties of zinc-oxide by investigating a ZnO thin film. We assume the sample to be transparent with negligible backside reflection. The resolution throughout these measurements were kept at 4 cm^{-1} .

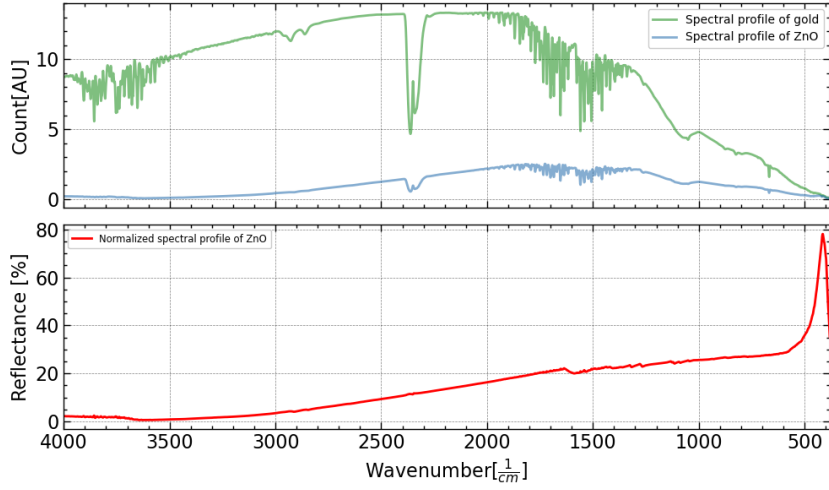


Figure 33: ZnO reflection spectra (blue) with reference gold (green), and ZnO reflection normalized to gold (red)

The reflectance increases steadily from the $3000 - 500 \text{ cm}^{-1}$ range, after which a significant contribution is made by the fingerprint region. The interaction of free charge carriers with electromagnetic radiation in semiconductors is primarily through intraband transitions, Drude absorption, and plasmon resonances. As ZnO is a wide band gap (3.37 eV at room temperature [23]) II-VI semiconductor with relatively low intrinsic free carrier concentration, we will limit our analysis to contributions from χ^L only. A fit on the reflectance spectrum in the fingerprint region can be performed using equation (56):

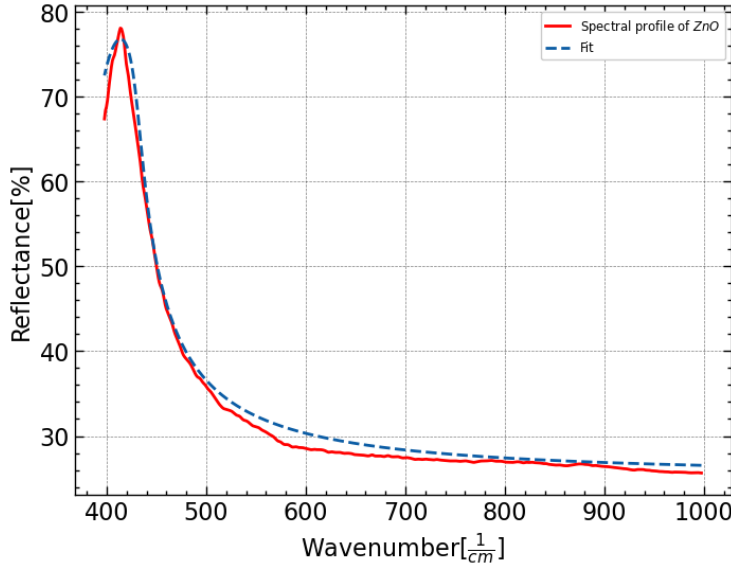


Figure 34: ZnO reflectance spectra fit

The fitting parameters we obtained are the following:

Parameters	Fitting values [cm^{-1}]
A	75.283 ± 0.4
ω_0	365.477 ± 0.674
η	17.383 ± 0.203
ε_∞	0.109 ± 0.001

Table 4: Table of fitting parameters

Calculated background dielectric $\varepsilon_\infty = 0.109 \pm 0.001$ is comparable to literature values of [24]. The obtained parameters from Table 4, allows us to plot the complex dielectric function:

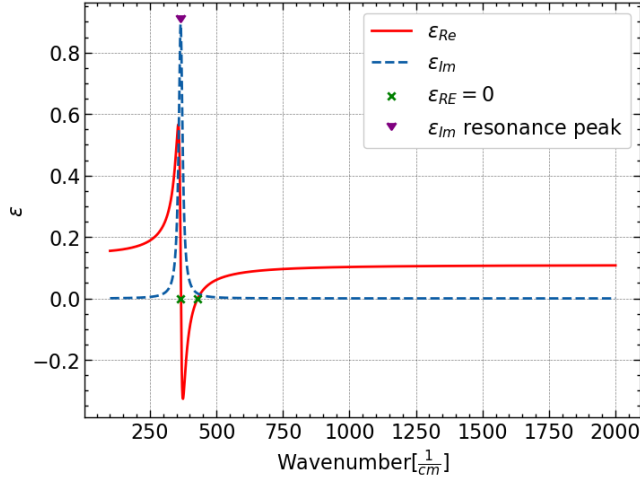


Figure 35: ZnO complex dielectric function

The following table shows the values at which $\text{Re}(\varepsilon) = 0$, and the resonance peak positions of $\text{Im}(\varepsilon)$:

Zero-crossing index	$\tilde{\nu} [cm^{-1}]$	Resonance peaks index
1	366.257 ± 0.001	1
2	430.083 ± 0.001	—

Table 5: Zero-crossing of $\text{Re}(\varepsilon)$ and resonance peaks of $\text{Im}(\varepsilon)$

We thus assign the TO mode from resonance wavenumber ω_0 from Table 5, and the LO mode from zero-crossing of $\text{Re}(\varepsilon)$ which yields:

Index (j)	$\tilde{\nu}_{LO} [cm^{-1}]$	$\tilde{\nu}_{TO} [cm^{-1}]$
1	366.257 ± 0.001	365.477 ± 0.674
2	430.083 ± 0.001	—

Table 6: Derived vibrational modes of ZnO

ZnO presents a Wurtzite structure with crystallization in the hexagonal P6₃mc group.

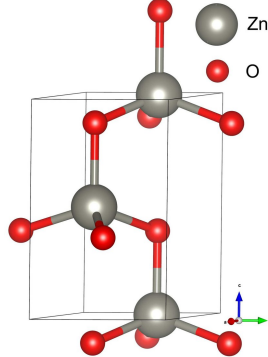


Figure 36: ZnO unit cell [25]

Active phonon modes between the corner sharing ZnO₄ tetrahedra are presented below:

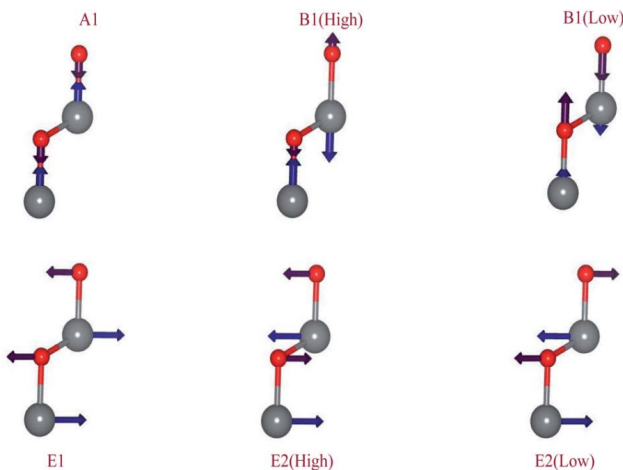


Figure 37: The identified modes of vibration of ZnO thin-films in IR and Raman spectra [26]

The B1 modes are silent in Raman and IR spectroscopy due to their symmetry, while the A1 and E1 are active in both Raman and IR. The E2 mode is active only in Raman. In this unit cell one expects to see 12 photonic modes with the following distribution: 6 TO, 3 LO, 2 TA, and 1 LA. Comparing Figure 37 and 36, we see that for A and B modes, displacements are directed along the c-axis.

The A mode consists of oscillations of Zn atom against the O atom, which induces a polarizing effect. B1 (high) refers to minimal motion of O atoms, while B1 (low) refers motion of the heavier Zn sublattice. As mentioned in the analysis of sapphire, the E modes carry out oscillations perpendicular to the c-axis with E1 exhibiting polarizing oscillations. E2 (low) mainly concerns the motion of

Zn sublattice with O sublattice contributions being in E2 (high). These latter modes are non-polar. Note that position of the measured bands and peaks not only depend on sample chemical composition and film structure, but also on the morphology [27]. The obtained $\tilde{\nu}_{TO}$ mode is 4% higher than an A1(TO) match from Venger (1995) [28]. Our LO mode around 430 cm^{-1} is consistent with E2 (high) mode from literature [29].

3.6 Task 6: Free Charge Carriers Asborption in GaAs

Our sample for this task is a doped n-type semiconductor Gallium Arsenide sample. The measured reflectance spectra is presented below:

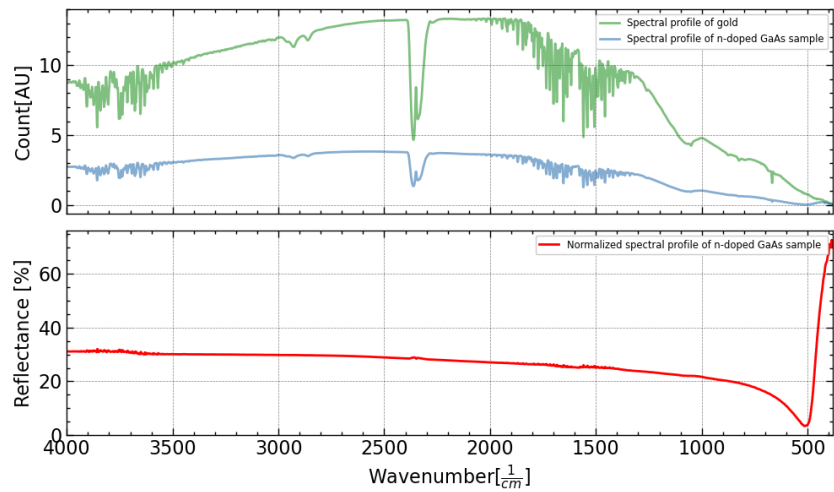


Figure 38: n-doped GaAs reflectance (blue) with reference gold foil (green), and n-doped GaAs reflectance normalized to gold foil (red)

Considering the presence of free carrier excitations, their contribution to the dispersion is of significant importance and will be given by the Drude term χ^P as discussed in equation (24). Additionally, optical-phonon modes in the $200\text{-}300\text{ cm}^{-1}$ range may be excited [32]. We will thus include one χ^L contribution, with our fitting equation being:

$$R = \left| \frac{1 - \sqrt{\varepsilon_\infty + \chi^L + \chi^P}}{1 + \sqrt{\varepsilon_\infty + \chi^L + \chi^P}} \right|^2 \quad (60)$$

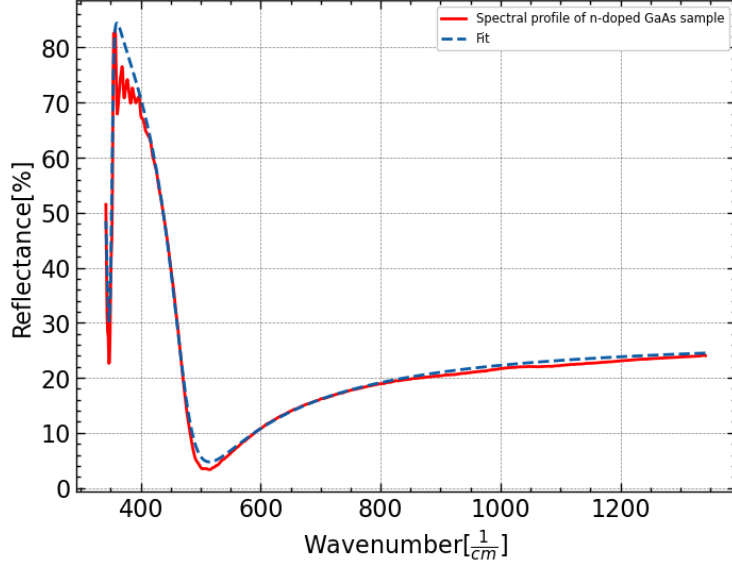


Figure 39: n-doped GaAs reflectance spectra fit

The fit results in the following parameters:

Parameters	Fitting values [cm^{-1}]
A	204.414 ± 1.966
ω_0	353.034 ± 0.087
η	3.814 ± 0.162
ε_∞	10.000 ± 0.029
ω_p	1480.860 ± 2.534
γ_e	66.666 ± 0.702

Table 7: Table of fitting parameters

Applying the condition for plasma resonance $\varepsilon(\omega'_p) = 0$ in the $\tau \rightarrow \infty$ limit,

$$\varepsilon_\infty - \frac{\omega_p^2}{\omega'^2_p} = 0 \implies \omega'_p = \frac{\omega_p}{\sqrt{\varepsilon_\infty}} \quad (61)$$

In materials with a high background dielectric constant, the electric field is more effectively screened by the bound electrons, reducing the effective interaction with the free carriers. This screening effect lowers the plasmon frequency. We thus have,

$$\omega'_p = 468.289 \pm 1.050 \text{ cm}^{-1}$$

From literature, the effective electron mass in GaAs is given by $m* = 0.067m_e$ [33]. Applying Equation 26 to get an estimation of the free charge carrier concentration,

$$n_s = (1.63804 \pm 0.007) \times 10^{18} \text{ cm}^{-3}$$

Intrinsic carrier concentration of GaAs is in the order of 10^6 cm^{-3} [34], implying that our sample is heavily doped with donors, as expected. From Figure 39 one

notices that for $\omega > \omega_p$, $\varepsilon > 0$, thus waves can propagate. For $\omega < \omega_p$ however, the dielectric constant is negative. The waves are exponentially damped and can not propagate through the material, causing a sharp increase in reflectance. This effect is exploited in plasmon waveguides [4]. The effect of carrier absorption is visualized below:



Figure 40: Czochralski-grown Ga₂O₃ crystals with different electron concentrations [4]

The blue hue of the boule with the higher electron concentration is due to free carrier absorption in the long wavelength part of the visible spectrum. The obtained $\tilde{\nu}_{TO} = 353 \text{ cm}^{-1}$ is above 20% of literature values of LO and TO modes of GaAs [32], possibly due to not incorporating the small LT split into the fit.

4 Conclusion & Outlook

After deriving a satisfactory calibration equation for the spectrometer in task 1, glass and NaCl blocking filters spectra were analyzed. A prediction about the chemical composition of the glass filter was made by qualitative judgement of the blocking strength bands. The Restrahlen effect in ionic crystals was observed in the far IR region of NaCl filter. The sapphire sample produced distinct features pertaining to phonon modes in the reflectance spectra, which were then related to known modes from group theory. However, a proper LT splitting was not achieved due to the fitting function being highly sensitive to initial guesses and not yielding reliable results. The sample thickness calculation was performed over two different regions of the spectra, each conforming to different ideal conditions. In task 4, the calculated absorption and extinction coefficient of Silicon were verified from a database. The phonon modes of ZnO thin film obtained in task 5 showed agreement with those reported in various papers. In the final section, charge carrier contribution to reflection was observed with the analysis yielding a very highly doped n-GaAs sample.

We propose intermittent IR exposure to measure spectra where absorption is expected to be high. This will minimize thermal noise within the sample, providing more accurate optical parameters.

References

- [1] Meggers W (1967). *W. William Weber Coblenz - A Biographical Memoir*. National Academy of Sciences
- [2] Zeitler JA. et. al. (February 2007). *Terahertz Pulsed Spectroscopy and Imaging in the Pharmaceutical Setting - A Review*. The Journal of Pharmacy and Pharmacology. 59 (2): 209–23. doi:10.1211/jpp.59.2.0008
- [3] Tsirlin A (January 29, 2024). *Introductory Solid-State Physics, Lecture Notes*. Leipzig University (URL: <https://research.uni-leipzig.de/sum/ssp.html>)
- [4] Grundmann, M. (2016). *The Physics of Semiconductors*. Springer
- [5] Peter Yu (2010). *Fundamentals of semiconductors: physics and materials properties*. Springer, Berlin New York
- [6] Instructions for Advanced Laboratory. *Lattice Vibrations and effects of free charge carriers*
- [7] Lee, J., Jin, J. *A novel method to design and evaluate artificial neural network for thin film thickness measurement traceable to the length standard*. Sci Rep 12, 2212 (2022). <https://doi.org/10.1038/s41598-022-06247-y>
- [8] Stuart, B. H. (2004). *Infrared spectroscopy: Fundamentals and Applications*. Wiley.
- [9] Hsu Sherman. C.-P. (2013) *Infrared spectroscopy*. MMRC Caltech.
- [10] Sturm. C. *Advanced Physics Laboratory: Lattice Vibrations and Effects of Free Charge Carriers in Solids*. (URL: https://home.uni-leipzig.de/physfp/versuche/git_e.html)
- [11] PerkinElmer Inc. (2011). *IR Ready To GO*. (URL: <https://www.perkinelmer.com/product/spectrum-two-ft-ir-sp10-software-l160000a>)
- [12] Dussauze, M. et. al. (2010). How does thermal poling affect the structure of soda-lime glass?. Journal of Physical Chemistry C. 114. 12754-12759.
- [13] The Nature of Vibrational Scpectroscopy. *Infrared Spectroscopy*. Michigan State University. (URL: <https://www2.chemistry.msu.edu/faculty/reusch/virttxtjml/spectrpy/infrared/irspecl.htm>
- [14] Herth, E. et. al. (2016). Investigation of amorphous SiO_x layer on gold surface for Surface Plasmon Resonance measurements. Microelectronic Engineering. 163. 10.1016/j.mee.2016.04.014.
- [15] Fox, Mark (2010). *Optical Properties of Solids (2nd ed.)*. Oxford University Press. ISBN 978-0199573370.
- [16] Stumpf, Wolfgang (2001). *Investigation and Simulation of the Optical Properties of Doped Silicon*. University of Constance

- [17] M. N. Polyanskiy. Refractiveindex.info database of optical constants. *Sci. Data* 11, 94 (2024) (<https://doi.org/10.1038/s41597-023-02898-2>) (URL: <https://refractiveindex.info/>)
- [18] A. K. Harman, S. Ninomiya, and S. Adachi, *J. Appl. Phys.* 76, 8032(1994)
- [19] F. Gervais and B. Piriou, *J. Phys. C* 7, 2374 (1974)
- [20] A. S. Barker, *Phys. Rev.* 132, 1474 (1963)
- [21] Crystallography matters...more! (2014), Crystallography365 (URL:https://www.iycr2014.org/learn/crystallography365/categories/inorganic-structures?result_105899_result_page=37)
- [22] Hortensius, Jorrit et. al. (2020). Tunable shear strain from resonantly driven optical phonons.
- [23] A. Mang, K. Reimann, St Rubenacke. *Solid State Commun.*, 94 (1995), p. 251
- [24] Rathnasekara et. al. (2022). "Thermoelectric, Electrochemical, & Dielectric Properties of Four ZnO Nanostructures" *Materials* 15, no. 24: 8816. <https://doi.org/10.3390/ma15248816>
- [25] Queiroz et. al. (2020). Structural and optical properties of Al-doped ZnO thin films produced by magnetron sputtering. *Processing and Application of Ceramics.* 14. 119-127. 10.2298/PAC2002119Q.
- [26] Moussa B.N.,et. al. Synthesis of ZnO sol-gel thin-films CMOS-Compatible. *RSC Advances*, 2021, 11 (37), (p.22723-22733)
- [27] Z. Yang, Z. Ye, Z. Xu and B. zhao, *Phys. E*, (2009), 42, (p. 116–119)
- [28] E. F. Venger, A. V. Melnichuk, L. Lu. Melnichuk, and Yu. A. Pasechnik, *Phys. Status Solidi B* 188, 823, (1995)
- [29] Ashkenov, N. et. al. (2003). Infrared Dielectric Functions and Phonon Modes of High-Quality ZnO Films. *Journal of Applied Physics.* 93. 126-133. 10.1063/1.1526935.
- [30] P.A. Fernandes, P.M.P. Salome, A.F. da Cunha, *J. Phys. D. Appl. Phys.* 43(21) (2010). 215403. 10.1088/0022-3727/43/21/215403.
- [31] Narayanan, S. et. al. (1997). Determination of unknown stress states in silicon wafers using microlaser Raman spectroscopy. *Journal of Applied Physics.* 82. 10.1063/1.366072.
- [32] Sparavigna, Amelia Carolina. (2015). Thermal Conductivity of Zincblende Crystals. *MECHANICS, MATERIALS SCIENCE & ENGINEERING JOURNAL.* 1. 28-35.
- [33] Zeghbrouck. B. (1997) Effective mass in semiconductors (URL:<https://apachepersonal.miun.se/~gorthu/halvledare/Effective%20mass%20in%20semiconductors.htm>)
- [34] Schlesinger. T.E. (2001) Encyclopedia of Materials: Science and Technology. ISBN 978-0-08-043152-9